Multidecadal Preconditioning of the Maud Rise Polynya Region

René M. van Westen[1] and Henk A. Dijkstra[1,2]

[1]Institute for Marine and Atmospheric research Utrecht, Department of Physics, Utrecht University, Utrecht, the Netherlands
[2]Center for Complex Systems Studies, Utrecht University, Utrecht, the Netherlands

Correspondence to: René van Westen <r.m.vanwesten@uu.nl>

Abstract. In this paper, we consider Maud Rise polynya formation in a long (250 years) high-resolution (ocean 0.1°, atmosphere 0.5° horizontal model resolution) of the Community Earth System Model. We find a dominant multidecadal time scale in the occurrence of these Maud Rise polynyas. Analysis of the results leads us to the interpretation that a preferred time scale can be induced by the variability of the Weddell Gyre, previously identified as the Southern Ocean Mode. The large-scale

5   pattern of heat content variability associated with the Southern Ocean Mode modifies the stratification in the Maud Rise region and leads to a preferred time scale in convection through preconditioning of the subsurface density, and consequently to polynya formation.

1 Introduction

A polynya is an open-water area enclosed by sea ice which persists at least for a few months. A famous area for polynya

10   formation is the Maud Rise region in the Weddell Sea. Polynyas occurring at this location are usually referred to Maud Rise Polynyas (MRPs), referring to the bathymetry feature below the ocean water. An MRP was well observed during the austral winters and springs of 1974 – 1976 by in situ (Gordon, 1978) and satellite microwave imaging (Carsey, 1980). The mid-1970s MRP was characterised by a sea-ice enclosed open water area ($1 - 3 \times 10^5$ km^2) located near 0°E and 65°S (Gordon, 1978). The interest for polynyas has increased recently because of the appearance of an MRP in the austral winter and spring of 2017,

15   with an open-water area of about 0.5×10^5 km^2 (Campbell et al., 2019).

Many observational, modelling and theoretical studies based on the 1974 – 1976 MRP have addressed its formation, evolution and decay (Martinson et al., 1981; Parkinson, 1983; Holland, 2001; Gordon et al., 2007; Martin et al., 2013; Latif et al., 2017; Weijer et al., 2017; Kurtakoti et al., 2018). The occurrence of convection below the region of the MRP is clearly a generic aspect during MRP formation. Convective events are induced by a destabilisation of the water column and the classical view

20   is that surface salinity anomalies (e.g. through brine rejection) induce convection once the column is preconditioned through subsurface processes (Martinson et al., 1981). In Gordon et al. (2007), it is proposed that a negative phase of the Southern Annular Mode (SAM) causes a negative freshwater flux leading to destabilisation of the water column. Preconditioning can, for example, occur due to the interaction of an ocean eddy and the Maud Rise topographic feature (Holland, 2001).

The occurrence of Southern Ocean convection is also ubiquitous in many global climate models (GCMs). Martin et al.

25   (2013) show that in the Kiel Climate Model (KCM) a centennial time scale build-up of a heat reservoir at mid-level depths (1000 – 3000 m) preconditions the water column affecting convection. Reintges et al. (2017) analysed a variety of (Coupled

Model Intercomparison Project phase five, CMIP5) GCMs and found that several models display deep convection events at multidecadal timescales, for example the GFDL-CM (Zanowski et al., 2015; Zhang and Delworth, 2016). Reintges et al. (2017) argue that models with a weak (strong) stable stratification tend to have a shorter (longer) re-occurrence time of deep convection, and demonstrate the importance of sea-ice volume on the average length of both non-convective and convective

5 periods.

Dufour et al. (2017) analysed MRP events in two versions (eddy-permitting and eddy-resolving) of the GFDL-CM. The lower resolution version has a weaker vertical background stratification (compared to the high-resolution version) and displays quasi-continuous deep convection events. The effects of eddy-driven heat- and salt transports and the representation of overflows were shown to be crucial for the stratification changes in the Maud Rise region (Dufour et al., 2017). In addition, Weijer et al. (2017)

10 demonstrated in a 100-year model simulation of the Community Earth System Model (CESM) that the MRP is only present in the eddying-version of the same model. The results in Dufour et al. (2017) and Weijer et al. (2017) suggest that ocean eddies (and also overflows) play a significant role in the vertical background stratification (in addition to the effects already mentioned by Reintges et al. (2017)) and therefore affect the time scale of the occurrence of deep convection.

The diverse multidecadal (Reintges et al., 2017) to centennial (Martin et al., 2013) variability found in climate models gives

15 the impression that convection can occur rather randomly through surface density perturbations once the water column is sufficiently preconditioned. However, recently rather regular multidecadal patterns of internal variability have been found in strongly eddying ocean models Le Bars et al. (2016). Analysis of the mechanism of this variability, the so-called Southern Ocean Mode (SOM), indicated that dynamical processes, involving eddy mean-flow interaction and eddy-topography interaction (Hogg and Blundell, 2006), are mainly responsible (Jüling et al., 2018). Recently, van Westen and Dijkstra (2017) have

20 shown that the SOM variability also occurs in a high-resolution ocean-eddying version of the CESM.

In this paper, we pursue the idea of the possible existence of a preferred multidecadal time scale of MRP events in the Southern Ocean through preconditioning and subsequent convection, by analysing the results of an extended CESM simulation as in van Westen and Dijkstra (2017). In this multi-century CESM simulation, several MRP events are found and we analyse the processes involved in these events. In Section 2, information on the CESM simulation and mean properties of the (Antarctic)

25 sea-ice field in the simulation are given. Analysis of the MRP events in CESM is provided in Section 3. A summary and discussion of the results with the main conclusions are given in the final Section 4.

2   Climate Model and Methods

The model output of CESM version 1.0.4 (Hurrell et al., 2013) is taken from the same simulation as used in van Westen and Dijkstra (2017), which has been extended for this study to model year 250. The ocean component (POP) and the sea-ice

30 component (CICE) of the model have a 0.1° horizontal resolution on a curvilinear, tripolar grid which captures the development and interaction of mesoscale eddies (Hallberg, 2013). The ocean model has 42 non-equidistant depth levels, with the highest vertical resolution near the surface. The atmosphere- and land surface components of CESM have a horizontal resolution of

a) GMST and net flux TOA

b) Global and Southern Hemispheric OHC
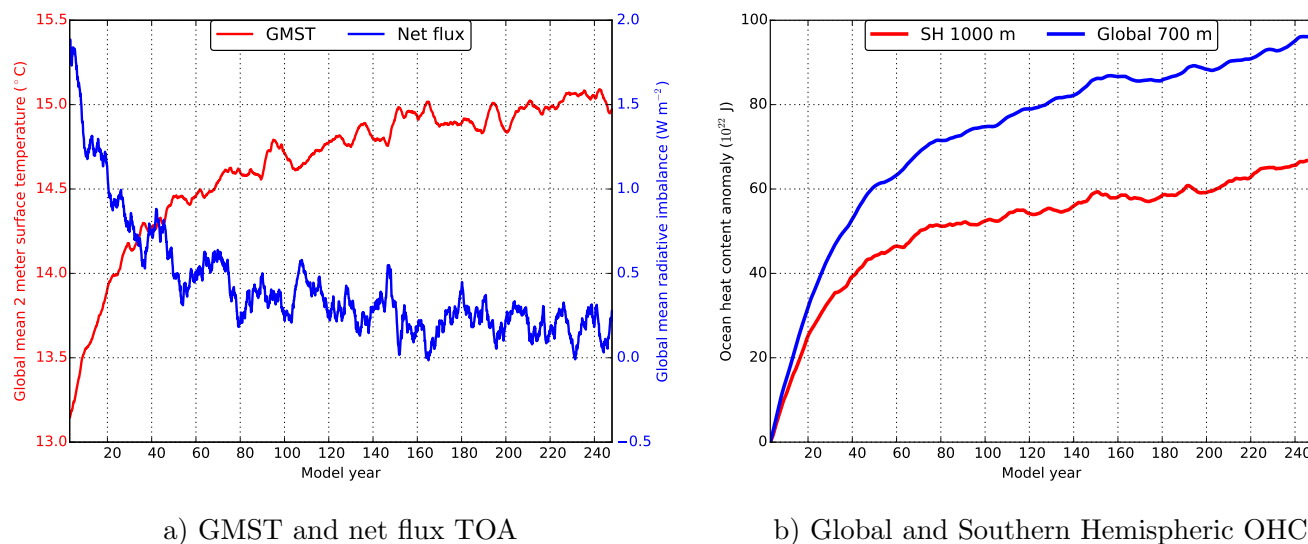
Figure 1. Equilibration of the CESM simulation for a) the global mean 2-meter surface temperature (GMST) and global radiative imbalance at the top of the model (Net flux) and in b) the upper 700 m global ocean heat content (OHC) anomaly and the upper 1000 m Southern Hemispheric OHC anomaly. The anomalies are with respect to their initial value of model year 1. All time series are smoothed by a 60-months running mean.

$0.5°$, and the atmosphere component has 30 non-equidistant pressure levels. The forcing conditions (e.g. CO_2, solar insulation, aerosols) are the observed ones over the year 2000 and are seasonally varying and repeated for every model year.

The equilibration of the CESM simulation over the first 250 model years is shown in Figure 1 (these results extend those in van Westen and Dijkstra (2017)). The global mean (2 meter) surface temperature and global mean radiative imbalance at the top of the atmosphere (Figure 1a) start equilibrating after about 150 years. The radiative imbalance is only slightly positive over the last 100 years of the simulation. The upper 700 m global ocean heat content and upper 1000 m Southern Hemispheric ocean heat content are still adjusting (Figure 1b), but relatively small trends (compared to the first part of the simulation) occur over the last 100 years which can easily be removed through a quadratic detrending. The deep ocean fields take a much longer time to equilibrate and hence the model state is not yet in equilibrium at year 250. Here, we analyse only the last 101 years (model years 150 – 250) of the simulation, using monthly averaged fields of the high-resolution output on the $0.1° \times 0.1°$ horizontal grid, instead of the interpolated output used in van Westen and Dijkstra (2017).

The time-mean September sea-ice extent (based on a minimum sea-ice fraction of 15%) is shown in Figure 2a as the black dashed curve and the modelled sea-ice extent reasonably agrees with observations (red dashed curve). For observations we used sea-ice measurements by the Scanning Multichannel Microwave Radiometer (SMMR) and Special Sensor Microwave Imager (SSM/I) (http://nsidc.org/data/G02202, Peng et al. (2013); Meier et al. (2017)). The time-mean September sea-ice thickness (colour plot in Figure 2a) displays relatively small values in the eastern part of the Weddell Sea. In this part of the Weddell Sea
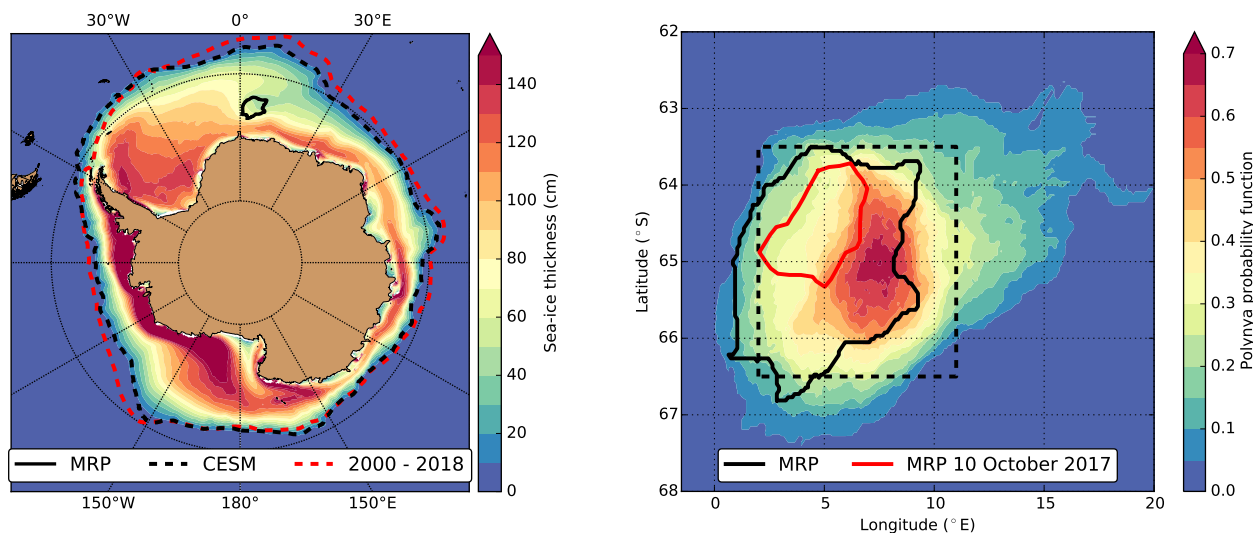
a) Average September sea-ice thickness

b) Polynya probability function

Figure 2. (a): Average sea-ice thickness (contours) for September over all the analysed years (model years 150 – 250) of the CESM output, including the time-mean September sea-ice extent (black dashed curve) and the time-mean (2000 – 2018) September sea-ice extent for SSMR-SSM/I. The September model year 181 MRP is shown by the black contour in a) and b). (b): Polynya probability function (explained in Section 2) based on all the polynya years. The dashed outlined region ($2°E – 11°E \times 63.5°S – 66.5°S$) is defined as the Polynya region. The observed 2017 MRP is indicated by the red contour in b).

multiple polynyas over Maud Rise appear in the CESM. In a companion CESM simulation, with a lower ocean resolution and sea-ice resolution of $1°$, no MRP formation is found over a simulated period of 1300 years (results not shown).

The MRP is defined as the enclosed region within the Antarctic sea-ice pack that has a sea-ice fraction smaller than 15% (Weijer et al., 2017). The observed 2017 MRP and a CESM modelled MRP are both located over Maud Rise (Figure 2b). The

5 MRPs found in CESM turn out to be quite localised in space and to determine that region, we computed a polynya probability density function. First, we define a polynya year to be a year where an MRP appears for at least three months. Secondly, at each MRP, the open-water grid cells (bounded by the 15% sea-ice fraction contour) and sea-ice covered grid cells are given a label of 1 and 0, respectively. This procedure is applied to each polynya year, so non-polynya years are discarded. Taking the average over all the labeled fields (0 or 1), results in the polynya probability density function as shown in Figure 2b. There is

10 a small region near $7.5°E$ and $65°S$ where there is open water for almost all MRPs. Based on the polynya probability density function, we define the Polynya region ($2°E – 11°E \times 63.5°S – 66.5°S$, shown as the dashed outlined region in Figure 2b).

We determined spatial averages over the Polynya region for the temperature, salinity, ocean heat content, sea-ice fraction, sea-ice thickness and the monthly maximum mixed layer depth. The mixed layer depth is defined as the depth at which the interpolated buoyancy gradient matches the maximum buoyancy gradient (this is standard output in CESM, Smith et al. (2010)).

The local ocean heat content (OHC), indicated by H_k, at model level z_k was calculated as:

$$H_k = \rho_k C_{p,k} T_k dz_k \tag{1}$$

where dz_k is the vertical cell length of the model grid at that level. The quantities ρ_k, T_k and $C_{p,k}$ are the local density, temperature and heat capacity, respectively. The temperature, salinity and pressure dependency are taken into account when

5 calculating the local density and heat capacity (Millero et al., 1980; Sharqawy et al., 2010).

The propagation of particles into the Polynya region is studied using OceanParcels (Probably A Really Computationally Efficient Lagrangian Simulator, version 2.1.4, Delandmeter and Van Sebille (2019)). In OceanParcels, one can release a set of virtual particles and track their path under the flow using Lagrangian modelling. Particles are passively advected by the time-varying 3D velocity field from the CESM output, either forward or backward in time. When a particle is released, its

10 age is set to zero and we removed particles from the particle set when they reach an age of 10 years. We used a time step of $\Delta t = 1$ hour to update the location of each particle (by linear interpolation of the velocity fields, Delandmeter and Van Sebille (2019)) and the output of each particle (i.e. age, depth, latitude and longitude) is stored every 10 days.

3 Results

In subsection 3.1 below, we first present the characteristics of the MRP events found in the CESM simulation. It turns out

15 that that there is a preferred multidecadal variability in MRP formation, possibly linked to the SOM (Le Bars et al., 2016), and this teleconnection is analysed in subsection 3.2. The processes causing the associated convective events, in particular the preconditioning of the density field are analysed in the last subsection 3.3.

3.1 Maud Rise Polynyas in the CESM

The September sea-ice fraction (blue curve in Figure 3a) shows relatively low sea-ice fractions with respect to the time-mean

20 for four periods: model years $158 - 159$, $178 - 182$, $205 - 209$ and $231 - 237$. These relatively low sea-ice fractions (as well as for the sea-ice thickness) are related to polynya formation over Maud Rise. The black curves in Figures 3b, c, d represent the annual maximum of the monthly maximum mixed layer depth averaged over the Polynya region. During MRP events, the mixed layer depth strongly increases over the Polynya region. A deepening of the mixed layer is also strongly correlated ($r = -0.98$) with a relatively low September sea-ice fraction over Maud Rise.

25 When the mixed layer deepens (i.e. during MRPs), heat and salinity anomalies are mixed towards the surface. The vertical distributions for the OHC, temperature and salinity anomalies over the Polynya region are displayed in Figure 3b, 3c and 3d, respectively. To determine these anomalies at depth z_k, first the time mean (over model years $150 - 250$) is subtracted from the time series and the result is quadratically detrended. The resulting time series (H_k, T_k and S_k for heat content, temperature and salinity, respectively) is smoothed using a 60-month moving average. Prior to each multiyear MRP event,

30 positive subsurface ($200 - 2000$ m) anomalies of OHC, temperature and salinity are found over the Polynya region (Figure 3,b, c and d, respectively).

a) OHC, SOM and sea-ice fraction

b) OHC and mixed layer depth

c) Temperature and mixed layer depth

d) Salinity and mixed layer depth
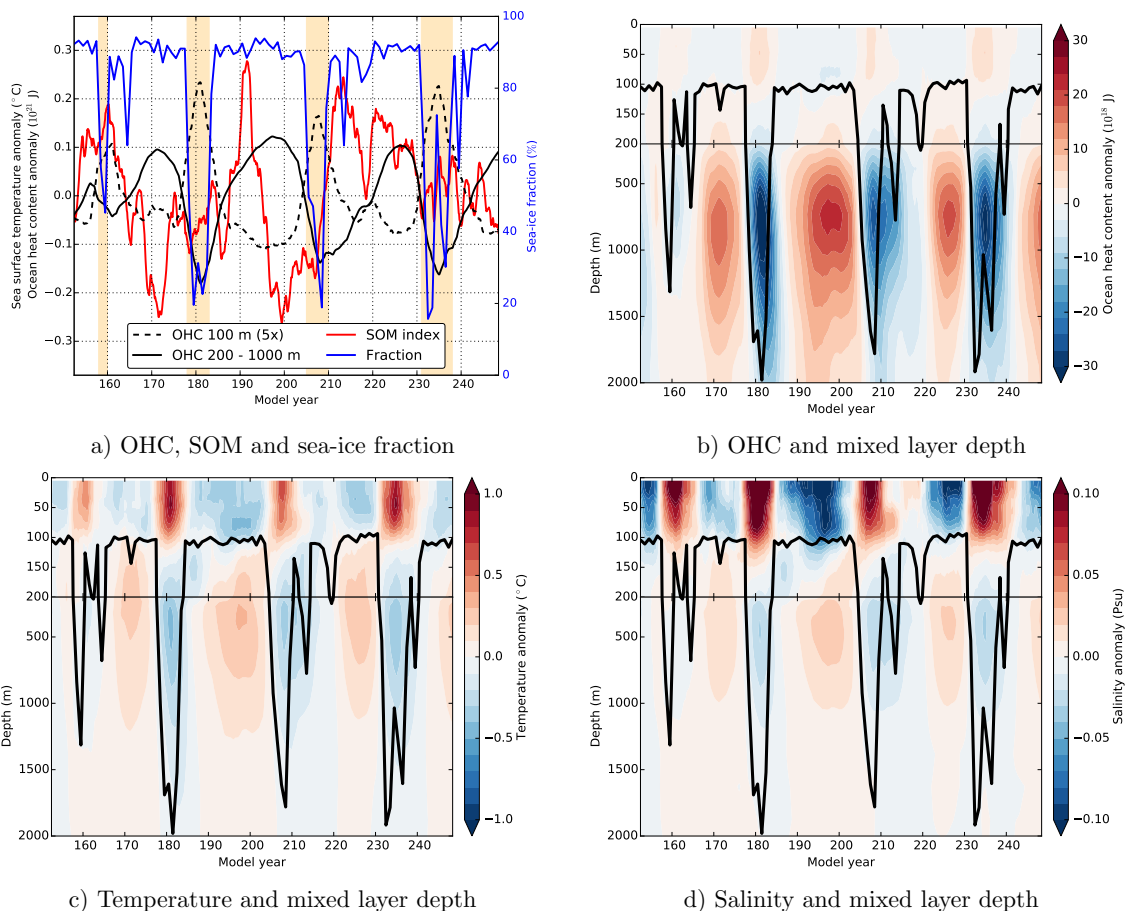
Figure 3. (a): Time series of the upper 100 m OHC anomaly ($\bar{H}_{100}$, magnified by a factor 5), the 200 − 1000 m OHC anomaly ($\bar{H}_{1000}$) and the September sea-ice fraction averaged over the Polynya region. The red curve is the SOM index. The OHC and SOM index time series are quadratically detrended and smoothed by a 60-months running mean. The shading indicates the polynya years. (b): Hovmöller diagram of the OHC anomaly vertical distribution (anomaly of OHC with respect to the time mean) over the Polynya region, smoothed by a 60-months running mean. The black curve indicates the annual maximum mixed layer depth. (c & d): Same as b), but now for the oceanic c) temperature and d) salinity.

a) Spectrum mixed layer depth   b) Spectrum SOM
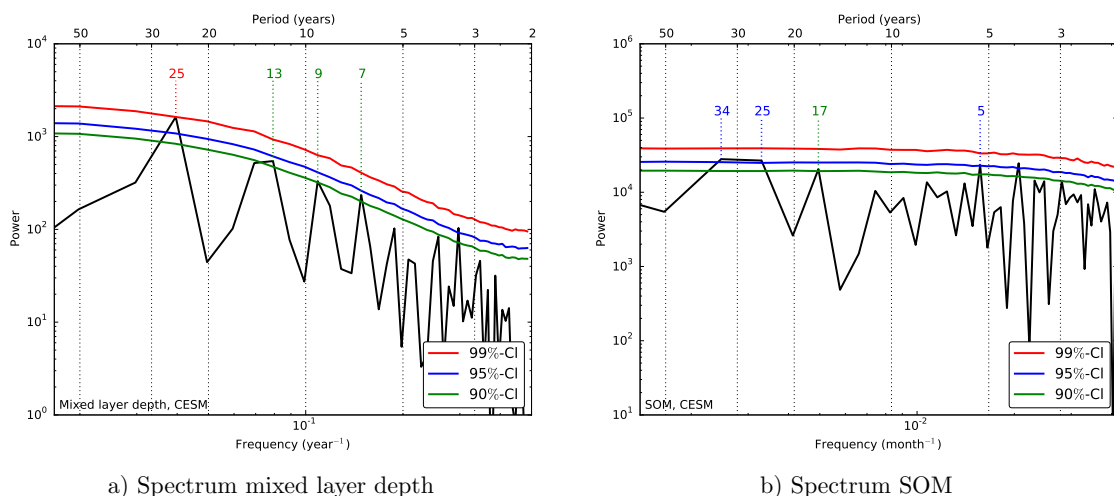
Figure 4. Fourier spectrum of the a) mixed layer depth averaged over the Polynya region and b) SOM index time series (the temperature anomaly over the region $0°W - 50°W \times 35°S - 50°S$). Before determining the spectrum, the yearly mixed layer depth time series is normalised (to the standard deviation). For the SOM index, the monthly averaged time series of the SOM index is (quadratically) detrended, the seasonal cycle is removed and the result is normalised (to the standard deviation). The confidence levels of significance (99% (red), 95% (blue) and 90% (blue)) are derived from 10000 surrogate time series. The indicated periods (in years) are significant at the corresponding colour-coded confidence level, while only indicating low-frequency periods (≥ 5 years).

On the contrary, the surface layer (upper 100 m) remains relatively cold and fresh prior to polynya formation. This decoupling of the surface and subsurface is also shown in Figure 3a for $\bar{H}_{100}$ and $\bar{H}_{1000}$, where we integrated the OHC anomalies over the upper 100 m and between $200 - 1000$ m depths, respectively. The time series of $\bar{H}_{100}$ and $\bar{H}_{1000}$ are $180°$ out of phase. During an MRP event, the mixed layer depth increases, positive subsurface heat and salt anomalies are mixed towards the surface

5   leading there to positive surface anomalies. The surface heat anomalies lead to sea-ice melt and consequently to polynya formation, in agreement with earlier studies (Martin et al., 2013; Dufour et al., 2017; Reintges et al., 2017).

The variability associated with the SOM can be measured via the SOM index which is defined as the temperature anomaly over the region $0°W - 50°W \times 35°S - 50°S$ (Le Bars et al., 2016). The SOM index (shown as the red curve in Figure 3a) displays also multidecadal variability. Fourier spectra of the mixed layer depth and SOM index are shown in Figure 4. The

10   dominant period of convection (i.e. deepening of the mixed layer depth) has a significant (99%-confidence level) 25-year period against red noise (Figure 4a). The time series of OHC, temperature, salinity and sea-ice fraction vary with the same multidecadal period as a consequence of convection (spectra not shown). The SOM index varies also on a dominant 25-year period which is significant (95%-confidence level) against red noise (Figure 4b). The possible connection between the SOM and the mixed layer depth variability is analysed in the following section.

3.2 SOM Related Variability in the Polynya Region

As demonstrated in the previous subsection, both the SOM index and the mixed layer depth over the Polynya region display multidecadal variability with the same dominant time scale. A lag-correlation analysis between the SOM index, $\bar{H}_{100}$ and $\bar{H}_{1000}$ averaged over the Polynya region (time series in Figure 3a) is shown in Figure 5a. There are significant lag-correlations

5 (95%-confidence level, taking into account the reduction of the degrees of freedom due to the running mean) between the SOM-index and $\bar{H}_{1000}$, where $\bar{H}_{1000}$ leads by about 10 years (114 months). At the similar time scale, negative correlations exists between $\bar{H}_{100}$ and the SOM index.

The correlation pattern of the SOM index and the $\bar{H}_{100}$ field (Figure 5b) at lag 0 shows overall positive (and significant) correlations centred around the SOM region. The same analysis, but now for the $\bar{H}_{1000}$ field (Figure 5c), shows overall positive

10 and significant correlations in the South Atlantic, mainly south- and eastward of the SOM region, and positive correlations enter the Weddell Gyre at 30°E. Comparing Figures 5b and Figure 5c indicates that the large-scale OHC pattern associated with the SOM extends across the Southern Ocean, both horizontally and vertically (Le Bars et al., 2016). The optimal lag-correlation between the SOM index and the $\bar{H}_{1000}$ over the Polynya region is reached after 114 months (Figure 5a), this lag-correlation pattern is shown in Figure 5d. Positive and significant lag-correlations are found in the southern part of the Weddell Gyre

15 indicating that subsurface heat anomalies related to the SOM propagate along the Weddell Gyre (Le Bars et al., 2016); this will be analysed in more detail below.

The time-mean flow near the Polynya region is westward and is set by the large-scale pattern of the Weddell Gyre (Figure 6a). Using OceanParcles (cf. section 2), we can determine the origin of the water mass of Maud Rise. Backtracking the particles (using the time-varying 3D velocity fields) shows that the particles mainly propagate along the Weddell Gyre and eventually

20 enter the Polynya region (Figure 6b). The particles are initially released at 200 m and 500 m depths in the Polynya region on December model year 250. One obtains different trajectories when the particles are released in, for example, December model year 249. Therefore, we released particles every 30 days in the Polynya region (each spaced by $0.25°$ and fixed initial depth) and we backtracked these particles using OceanParcels over the CESM output (model years $150 - 250$).

The final distributions of all the particles backtracked for 8 years (i.e. an age of 2920 days) which are initially released at

25 200 m, 500 m and 1000 m depths in the Polynya region, are shown in Figure 7a, c and e, respectively. These results indicate that most particles propagate (backwards) along the Weddell Gyre (similar as the trajectories in Figure 6b) with little dependence on the initial depth . Note that the final distributions overlap with the positive correlations between the SOM and the $\bar{H}_{1000}$ field (Figure 5c). The backward propagation of the particles along the Weddell Gyre can also be identified using the colour-coded regions (as in Figure 7a, c and e). Here we determine the fraction of particles inside a specific region at a given age (Figure 7b,

30 d and f). All particles are released in the black-outlined region (this region slightly extends the Polynya region), and hence all particles have zero age. The time-mean flow in the black-outlined region is directed westwards (Figure 6a) which explains the relatively high ($\approx 70\%$) abundance of particles in the blue-outlined region after 2 years of backtracking. Via the blue dashed region, most ($> 50\%$) particles end up in the red region (i.e. south of the SOM region) after about $8 - 10$ years.
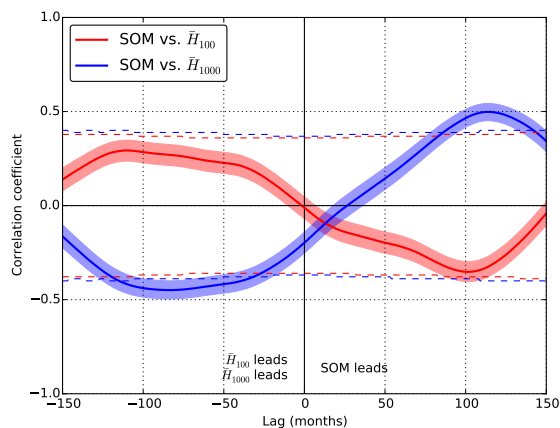
a) Lag-correlation analysis
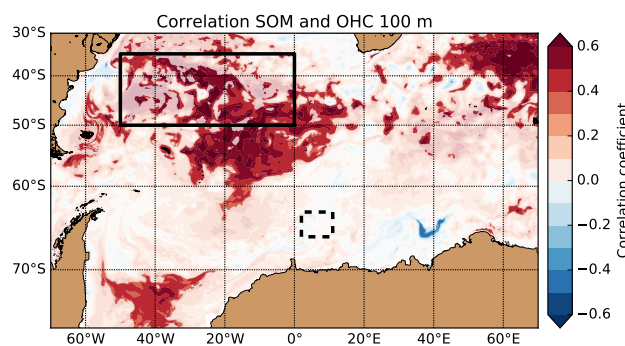
b) Correlation SOM and $\bar{H}_{100}$
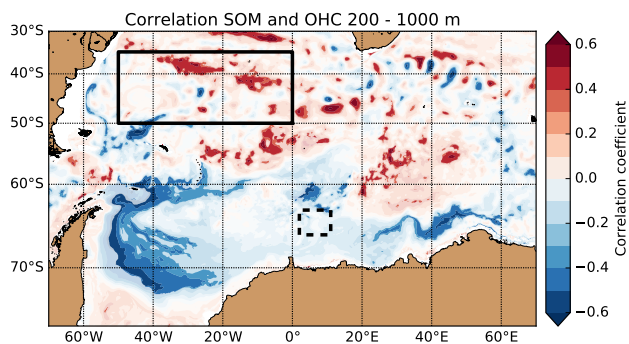
c) Correlation SOM and $\bar{H}_{1000}$
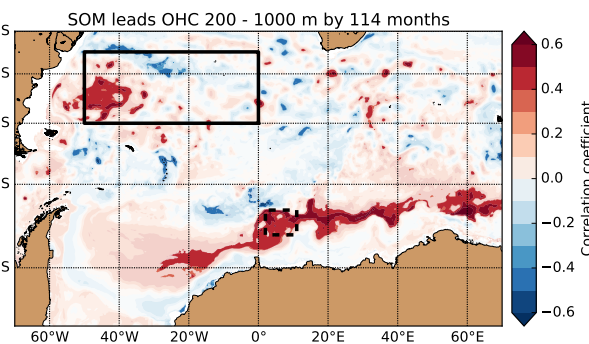
d) SOM leads $\bar{H}_{1000}$ by 114 months

Figure 5. (a): Lag-correlation analysis of the SOM index, the upper 100 m OHC anomaly ($\bar{H}_{100}$) and the 200 – 1000 m OHC anomaly ($\bar{H}_{1000}$), averaged over the Polynya region (see time series in Figure 3a). A positive (negative) lag indicates that the SOM time series leads (lags) the OHC time series. The shading indicates the 95%-confidence interval of lag-correlation, the dashed lines indicate the 95%-significant level. (b – c): Spatial correlation pattern of the SOM index time series and b) the $\bar{H}_{100}$ field and c) the $\bar{H}_{1000}$ field for zero lag. All time series are detrended and smoothed by a 60-months running mean before determining the lag-correlation. The black outlined region is the SOM region and the dashed outlined region the Polynya region. The darker coloured correlations indicate significant (95%-confidence level) correlations. (d): Same as c), but the SOM index time series leads the $\bar{H}_{1000}$ field by 114 months.

a) Horizontal velocity field 200 − 1000 m   b) Trajectories particles
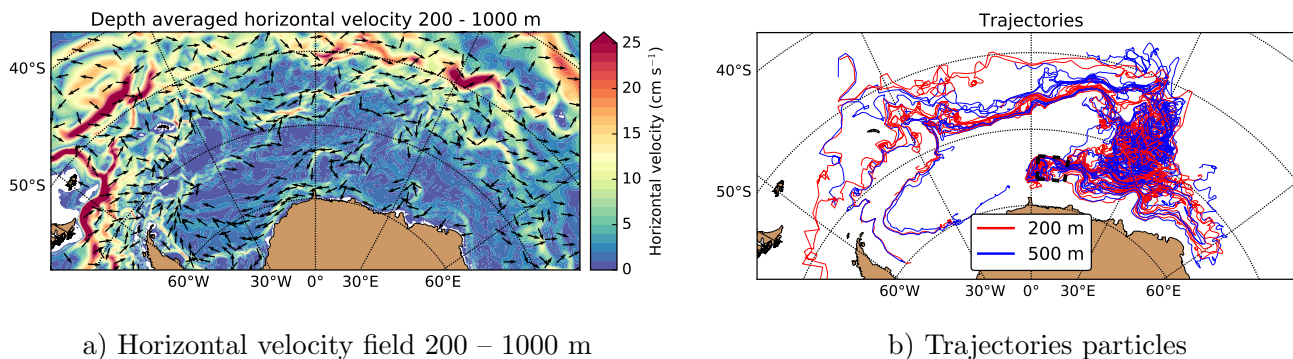
Figure 6. (a): Time-mean (model years 150 − 250) horizontal velocity field (arrows) between 200 − 1000 m depths, with the speed indicated in the contours. The arrows indicate the direction of the flow (not to scale) and are only shown for speeds larger than 2 cm s^{-1}. (b): The backtracked trajectories for some particles which are initially released at 200 m (red curves) and 500 m (blue curves) depths in the Polynya region (dashed outlined region).

The interpretation of these results is that when the SOM is in a positive phase, positive subsurface OHC anomalies are found south and eastward of the SOM region (Figure 5c). These anomalies subsequently reach the Polynya region after about 10 years (Figure 5d). In this way, the subsurface OHC anomalies are advected along the Weddell Gyre and enter the Polynya region (Figures 6 and 7).

3.3 Preconditioning of the Polynya Region

The propagation of subsurface OHC anomalies associated with the SOM causes subsurface heat accumulation in the Polynya region and leads to changes in the subsurface heat reservoir. The horizontal advective heat flux, indicated by $\boldsymbol{F}_k$, at model level z_k, was calculated as:

$$\boldsymbol{F}_k = \rho_k C_{p,k} \boldsymbol{u}_k T_k \, , \tag{2}$$

where $\boldsymbol{u}_k$ is the horizontal velocity vector at depth z_k. The zonal heat input at the eastern boundary (F_k^{East}) of the Polynya region (i.e. the normal component of $\boldsymbol{F}_k$ multiplied by the area perpendicular to the normal) with depth also displays multidecadal variability (Figure 8a). At mid-level depths, heat is advected into the Polynya region with the largest magnitudes occurring at depths between 700 − 900 m. This maximum in heat advection between 700 − 900 m depths is related to the maximum westward velocity which also occurs at subsurface depths. Positive (negative) values of F_k^{East} indicate heat advection into (out of) the Polynya region.

The subsurface heat reservoir increases when there is net heat accumulation over the Polynya region boundaries. The development of heat input for the different boundaries and the net effect of the Polynya region prior to the last multiyear MRP event, is shown in Figure 8c. In addition, the temperature difference between subsurface ($\bar{T}_{1000}$, 200 − 1000 m depths) and

a) Distribution after 8 years, initial depth 200 m

b) Distribution regions, initial depth 200 m

c) Distribution after 8 years, initial depth 500 m

d) Distribution regions, initial depth 500 m

e) Distribution after 8 years, initial depth 1000 m

f) Distribution regions, initial depth 1000 m
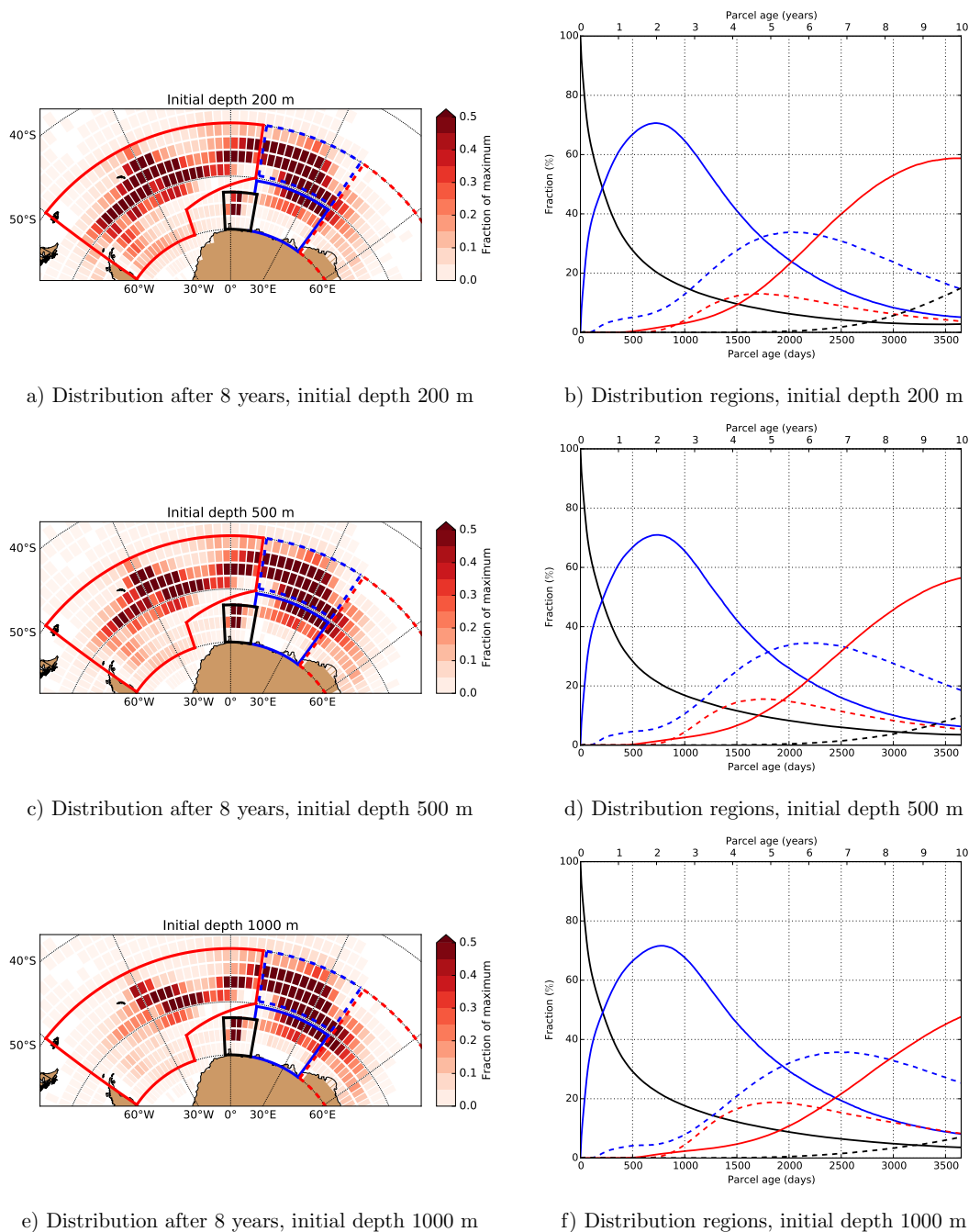
Figure 7. (a): Distribution of particles in the Southern Ocean after backtracking the particles for 8 years. The particles are initiated in the Polynya region at 200 m depth every 30 days. The colour-coded regions are used in b), where the red dashed region has a zonal extent of $60°$ ($40°$E – $100°$E). (b): The time evolution of the fraction of particles in the colour-coded regions (see a)). The black dashed curve are particles outside the defined regions. (c – f): Similar as a) and b), but the particles are initially released at 500 m and 1000 m depths in the Polynya region.
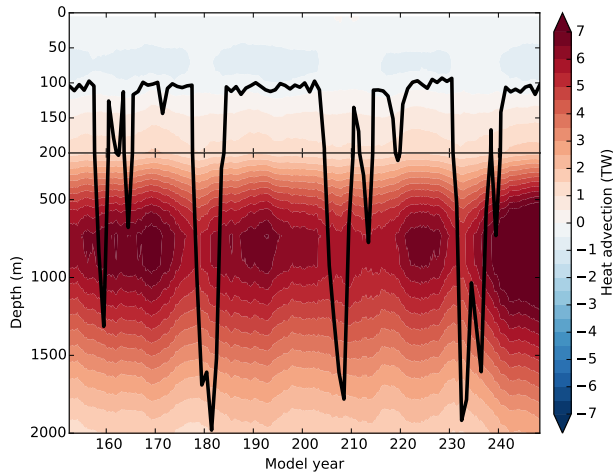
a) Advective heat and mixed layer depth
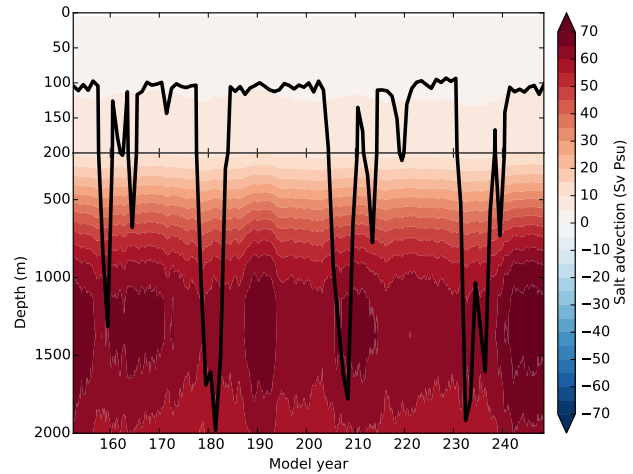
b) Advective salt and mixed layer depth
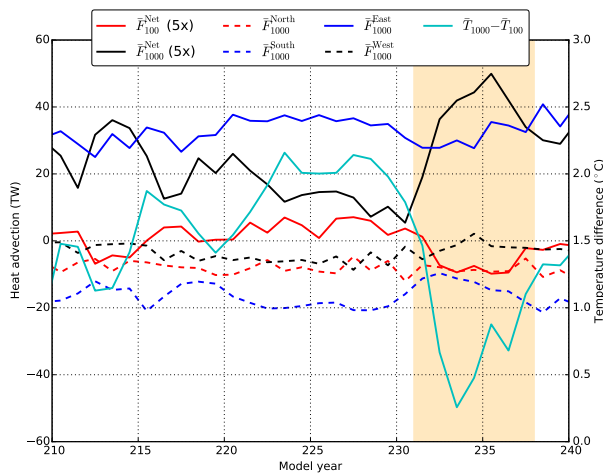
c) Advective heat
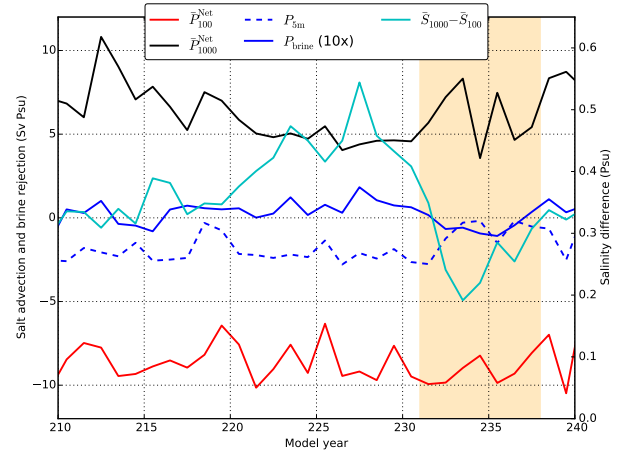
d) Advective salt and brine rejection

Figure 8. (a): Hovmöller diagram of the vertical distribution of heat input along the eastern boundary of the Polynya region ($11°$E, $63.5°$S $- 66.5°$S). Positive (negative) values indicate heat advection into (out of) the Polynya region. The time series are smoothed by a 60-months running mean. The black curve again indicates the (annual maximum) mixed layer depth of the Polynya region. (b): Similar to a), but now for the salt input. (c): The horizontal heat input over the Polynya region boundaries over the model years $210 - 240$, where positive (negative) values of $\bar{F}$ indicate accumulation (depletion) of heat in the Polynya region over the corresponding vertical extent. The net horizontal heat input over the Polynya region boundaries are indicated by $\bar{F}^{\mathrm{Net}}$ (magnified by a factor 5) over the corresponding vertical extent. The cyan curve is the temperature difference between subsurface ($\bar{T}_{1000}$) and surface ($\bar{T}_{100}$) over the Polynya region. All the time series consists of yearly averages and the shading indicates the last multiyear MRP event. (d): Similar to c), but now for the net advective salt input ($\bar{P}_{100}^{\mathrm{Net}}$ and $\bar{P}_{1000}^{\mathrm{Net}}$). The cyan curve is the salinity difference between subsurface ($\bar{S}_{1000}$) and surface ($\bar{S}_{100}$) over the Polynya region. In addition, the advective salt input of the surface layer (5 m, $P_{5\mathrm{m}}$) and the amount of salt due to brine rejection (P_{brine}, magnified by a factor 10), averaged over June – July for each year.

surface ($\bar{T}_{100}$, upper 100 m) averaged over the Polynya region is shown in Figure 8c, which is measure for the magnitude of the subsurface heat reservoir.

In model years 210 – 215, shortly after the third multiyear MRP event, the heat reservoir is depleted and the temperature difference is relatively small compared to the 5 years (225 – 230) before the 231 – 237 MRP. Between model years 210 – 230,

5 $\bar{F}_{1000}^{\text{Net}}$ is positive and larger compared to $\bar{F}_{100}^{\text{Net}}$, leading to an increase in the vertical temperature difference. As the temperature difference increases, the total amount of subsurface heat advected out (sum of $\bar{F}_{1000}^{\text{North}}$, $\bar{F}_{1000}^{\text{South}}$ and $\bar{F}_{1000}^{\text{West}}$) of the Polynya region also increases, consequently the net heat input $\bar{F}_{1000}^{\text{Net}}$ decreases over time. The time series (model years 150 – 250) of the temperature difference and $\bar{F}_{1000}^{\text{Net}}$ are significantly anti-correlated (95%-confidence level, $r = -0.88$). The build up of the subsurface heat reservoir weakens the stratification over the Polynya region. During polynya formation, heat is vertically mixed

10 causing a near zero temperature difference which indicates that the upper 1000 m is well mixed. Once convection ceases, the temperature difference returns to values of about 1.5°C (which is comparable to the values in model year 210) and the build-up of the heat reservoir starts all over again.

Preconditioning of the Polynya region also occurs by advection of salinity anomalies into the Polynya region and the advective salt fluxes are given by

$$\boldsymbol{P}_k = \rho_k \boldsymbol{u}_k S_k \ , \tag{3}$$

The salt input at the eastern boundary (P_k^{East}) of the Polynya region with depth is shown in Figure 8b. Here we expressed the salt input in units of Sv Psu (1 Sv $\equiv 10^6$ m³ s⁻¹), where 1 Sv Psu is about 10^9 g of salt per second. At the eastern boundary, salt is advected into the Polynya region over the upper 2000 m and the largest magnitude of salt advection is found between 1000 – 1500 m depths.

20 The eastern boundary contributes to subsurface salt accumulation in the Polynya region (Figure 8b), the other three boundaries (not shown) advect salt out of the Polynya region. The sign of $\bar{P}_{100}^{\text{Net}}$ and $\bar{P}_{1000}^{\text{Net}}$ are opposite, leading to an increase in the salinity difference between the subsurface ($\bar{S}_{1000}$, 200 – 1000 m) and surface ($\bar{S}_{100}$, upper 100 m) over the Polynya region prior to MRP formation (Figure 8d). An increase in the vertical salinity gradient, strengthens the stratification of the Polynya region. A saline surface layer (due to brine rejection) weakens the stratification, potentially leading to convection (Martin-

25 son et al., 1981). Therefore, we estimated the salt input from sea-ice formation or melt to the ocean surface using the virtual surface salt flux (standard output in the CESM) over the Polynya region. The virtual salt flux is derived from the freshwater flux (kg m⁻² s⁻¹) which is related to the difference in precipitation and evaporation, including some other processes (sea-ice formation, melt, run-off). When the Polynya region is sea-ice covered, the virtual salt flux is dominated by brine rejection or sea-ice melt, since the contribution of precipitation and evaporation tend to zero. The virtual salt flux is an order of magnitude

30 larger compared to precipitation and evaporation when sufficient sea-ice is present.

The total salt input by brine rejection to the ocean surface per grid cell, was calculated as:

$$P_{\text{brine}} = \frac{F_{\text{vsf}}}{\rho_0} S_0 A. \tag{4}$$

where the quantities A, S_0, ρ_0 and F_{vsf} are the local area of the grid cell, surface salinity, density of freshwater (1000 kg m⁻³) and virtual salt flux, respectively. For convenience and comparison, we expressed P_{brine} in units of Sv Psu. Note that during

MRP events and sea-ice free periods, the virtual salt flux is dominated by precipitation and evaporation and thus not representative for brine rejection. Therefore, we only retained the mean of P_{brine} over the period June – July for each year, when the grid cells in the Polynya region are most of the time sea-ice covered and the sea-ice rapidly grows. The time series of P_{brine} is also shown in Figure 8d.

5   The amount of salt input due to brine rejection (P_{brine}) is positive during non-polynya years, leading to an increase in salinity of the ocean surface layer over the Polynya region. During polynya years, P_{brine} is negative which is not related to brine rejection (as explained above). When omitting the MRP years, the time mean of P_{brine} is 0.07 Sv Psu over the Polynya region (0.05 Sv Psu when including the MRP years). The accumulated salt by brine rejection near the surface can be advected out of the Polynya region. Therefore, we included the net advective salt input (P_{5m}) of the surface layer (5 m) over the Polynya region boundaries while taking the mean over June – July for each year, to compare to P_{brine} (see also Figure 8d). The magnitude of salt input by brine rejection is much smaller compared to the advective salt output by $\bar{P}_{5m}^{\mathrm{Net}}$ = -1.7 Sv Psu (mean over all years). Brine rejection weakens the stratification near the surface, while changes in the vertical salinity gradient are mainly determined by horizontal (sub)surface advection of salt.

Based on this analysis of CESM results, the preconditioning of the density field seems to be most affected by the subsurface heat anomalies. Positive subsurface heat and salt anomalies, advected via the Weddell Gyre, increase the vertical gradient in temperature and salinity over the Polynya region, respectively. The increased vertical temperature (salinity) gradient weakens (strengthens) the stratification near Maud Rise.

4   Summary and Discussion

In this paper, we analysed the last 100 years of model output from a multi-century (250 years) control simulation of a high-resolution version of CESM under a repeated seasonal forcing of the year 2000. We find four multiyear MRP events and, in each event, (deep) convection causes vertical mixing of anomalous subsurface heat towards the surface where it melts the sea-ice and leads to the formation of the MRP. These processes of the formation and lifecycle of the MRP are broadly in agreement with the classical view as in Martinson et al. (1981) and those described from other model results in Martin et al. (2013), Dufour et al. (2017) and Reintges et al. (2017).

In the CESM, we find that the preconditioning of the subsurface density can be linked to an intrinsic dynamical ocean mode in the Southern Ocean, the SOM, which is dominantly caused by eddy-mean flow interaction (Jüling et al., 2018). A positive phase of the SOM leads to positive subsurface OHC anomalies in the South Atlantic Ocean Le Bars et al. (2016). These anomalies enter the Weddell Gyre near 30°E and, after about 10 years, they reach the Polynya region, where they cause deep convection and sea-ice melt. Hence, the frequency of occurrence of the MRP events is related to the SOM variability through the advection of the subsurface OHC anomalies in the Weddell Sea. In this case, a preferred frequency of convective events is induced through preconditioning, which is around 25 years in the CESM.

Changes in the vertical stratification lead to a different SOM period, which can already be seen in our CESM simulation results. van Westen and Dijkstra (2017) find in the first 200 years of this simulation a period of about 40 – 50 years, which is

similar to that found in the ocean-only (POP) model results of Le Bars et al. (2016). The meridional slope of the isopycnals increases (near 50°S) over time in the CESM simulation (not shown), which enhances the baroclinic flow and reduces the period of the SOM. The background density profiles in the CESM output also have a larger meridional isopycnal slope compared to the POP output (not shown) and hence one would indeed expect a longer period in POP compared to CESM. The zonal

5   thermal-wind component near 50°S in CESM is about 1.6 times stronger compared to that of POP.

Although preconditioning of the density field in the Maud Rise region is connected to subsurface advection of heat and salt anomalies, it does not strictly imply polynya formation. However, it will favour the occurrence of MRPs due to atmospheric variability, such as intense winter storms. For example, the formation of the 2016 – 2017 MRP was initiated by an increased storm frequency under the influence of a positive SAM index (Campbell et al., 2019). In the CESM, the SAM index is in a

10   positive phase prior to the second (178 – 182), third (205 – 209) and fourth (231 – 237) multiyear MRP (not shown), but the initiation process of the MRPs is out of the scope of this study.

Observations are unfortunately too sparse to falsify the hypothesis of a preferred multidecadal variability in the Southern Ocean. Relatively low sea-ice fractions were observed over Maud Rise in the mid-1970s, 1994 and 2016 – 2017, indicating a 20-year period in MRP formation (Lindsay et al., 2004; Gordon et al., 2007; Campbell et al., 2019) which reasonable agrees

15   with the 25-year period of the MRP formation in the CESM. If this view is correct and a preferred frequency in the Southern Ocean exists, it would imply that a next MRP event, if not affected by climate change (De Lavergne et al., 2014), can be expected by the mid-2030s.

Acknowledgements. The authors thank Michael Kliphuis (IMAU, UU) for performing the CESM simulations. The computations were performed on the Cartesius at SURFsara in Amsterdam. Use of the Cartesius computing facilities was sponsored by the Netherlands Organization

20   for Scientific Research (NWO) under the project 15552. The data from the model simulation used in this work is available upon request from the authors. The NOAA/NSIDC provided the satellite sea-ice products (http://nsidc.org/data/G02202). The OceanParcels framework can be obtained online (oceanparcels.org) and we thank Peter Nooteboom (IMAU, UU) for his assistance in setting up this code for the CESM data.

References

Campbell, E. C., Wilson, E. A., Moore, G. K., Riser, S. C., Brayton, C. E., Mazloff, M. R., and Talley, L. D.: Antarctic offshore polynyas linked to Southern Hemisphere climate anomalies, Nature, 570, 319–325, 2019.

Carsey, F.: Microwave observation of the Weddell Polynya, Monthly Weather Review, 108, 2032–2044, 1980.

5 De Lavergne, C., Palter, J. B., Galbraith, E. D., Bernardello, R., and Marinov, I.: Cessation of deep convection in the open Southern Ocean under anthropogenic climate change, Nature Climate Change, 4, 278–282, 2014.

Delandmeter, P. and Van Sebille, E.: The Parcels v2. 0 Lagrangian framework: new field interpolation schemes, Geoscientific Model Development, 12, 3571–3584, 2019.

Dufour, C. O., Morrison, A. K., Griffies, S. M., Frenger, I., Zanowski, H., and Winton, M.: Preconditioning of the Weddell Sea polynya by 10 the ocean mesoscale and dense water overflows, Journal of Climate, 30, 7719–7737, 2017.

Gordon, A. L.: Deep antarctic convection west of Maud Rise, Journal of Physical Oceanography, 8, 600–612, 1978.

Gordon, A. L., Visbeck, M., and Comiso, J. C.: possible link between the Weddell Polynya and the Southern Annular Mode, Journal of Climate, 20, 2558–2571, 2007.

Hallberg, R.: Using a resolution function to regulate parameterizations of oceanic mesoscale eddy effects, Ocean Modelling, 72, 92–103, 15 2013.

Hogg, A. M. C. and Blundell, J. R.: Interdecadal variability of the Southern Ocean, Journal of physical oceanography, 36, 1626–1645, 2006.

Holland, D.: Explaining the Weddell Polynya–a large ocean eddy shed at Maud Rise, Science, 292, 1697–1700, 2001.

Hurrell, J. W., Holland, M. M., Gent, P. R., Ghan, S., Kay, J. E., Kushner, P. J., Lamarque, J.-F., Large, W. G., Lawrence, D., Lindsay, K., et al.: The community earth system model: a framework for collaborative research, Bulletin of the American Meteorological Society, 94, 20 1339–1360, 2013.

Jüling, A., Viebahn, J. P., Drijfhout, S. S., and Dijkstra, H. A.: Energetics of the Southern Ocean Mode, Journal of Geophysical Research: Oceans, p. Accepted, 2018.

Kurtakoti, P., Veneziani, M., Stössel, A., and Weijer, W.: Preconditioning and formation of Maud Rise polynyas in a high-resolution Earth system model, Journal Of Climate, 31, 9659–9678, 2018.

25 Latif, M., Martin, T., Reintges, A., and Park, W.: Southern Ocean Decadal Variability and Predictability, Current Climate Change Reports, 3, 163–173, 2017.

Le Bars, D., Viebahn, J. P., and Dijkstra, H. A.: A Southern Ocean mode of Multidecadal Variability, Geophysical Research Letters, 43, 2102–2110, 2016.

Lindsay, R., Holland, D., and Woodgate, R.: Halo of low ice concentration observed over the Maud Rise seamount, Geophysical research 30 letters, 31, 2004.

Martin, T., Park, W., and Latif, M.: Multi-centennial variability controlled by Southern Ocean convection in the Kiel Climate Model, Climate dynamics, 40, 2005–2022, 2013.

Martinson, D. G., Killworth, P. D., and Gordon, A. L.: A convective model for the Weddell Polynya, Journal of Physical Oceanography, 11, 466–488, 1981.

35 Meier, W., Fetterer, F., Savoie, M., Mallory, S., Duerr, R., and Stroeve, J.: NOAA/NSIDC climate data record of passive microwave sea ice concentration, Version 3, National Snow and Ice Data Center, Boulder, CO. Available online at http://nsidc.org/data/docs/noaa/g02202_ice_conc_cdr/., 2017.

Millero, F. J., Chen, C.-T., Bradshaw, A., and Schleicher, K.: A new high pressure equation of state for seawater, Deep Sea Research Part A. Oceanographic Research Papers, 27, 255–264, 1980.

Parkinson, C. L.: On the development and cause of the Weddell Polynya in a sea ice simulation, Journal of Physical Oceanography, 13, 501–511, 1983.

5 Peng, G., Meier, W., Scott, D., and Savoie, M.: A long-term and reproducible passive microwave sea ice concentration data record for climate studies and monitoring, Earth System Science Data, 5, 311–318, 2013.

Reintges, A., Martin, T., Latif, M., and Park, W.: Physical controls of Southern Ocean deep-convection variability in CMIP5 models and the Kiel Climate Model, Geophysical Research Letters, 2017.

Sharqawy, M. H., Lienhard, J. H., and Zubair, S. M.: Thermophysical properties of seawater: a review of existing correlations and data, 10 Desalination and water Treatment, 16, 354–380, 2010.

Smith, R., Jones, P., Briegleb, B., Bryan, F., Danabasoglu, G., Dennis, J., Dukowicz, J., Eden, C., Fox-Kemper, B., Gent, P., et al.: The parallel ocean program (POP) reference manual ocean component of the community climate system model (CCSM) and community earth system model (CESM), Rep. LAUR-01853, 141, 1–140, 2010.

van Westen, R. M. and Dijkstra, H. A.: Southern Ocean Origin of Multidecadal Variability in the North Brazil Current, Geophysical Research 15 Letters, 44, 10,540–10,548, 2017.

Weijer, W., Veneziani, M., Stössel, A., Hecht, M. W., Jeffery, N., Jonko, A., Hodos, T., and Wang, H.: Local atmospheric response to an open-ocean polynya in a high-resolution climate model, Journal of Climate, 30, 1629–1641, 2017.

Zanowski, H., Hallberg, R., and Sarmiento, J. L.: Abyssal ocean warming and salinification after Weddell Polynyas in the GFDL CM2G coupled climate model, Journal of Physical Oceanography, 45, 2755–2772, 2015.

20 Zhang, L. and Delworth, T. L.: Impact of the Antarctic bottom water formation on the Weddell Gyre and its northward propagation characteristics in GFDL CM2.1 model, Journal of Geophysical Research: Oceans, 121, 5825–5846, 2016.